

HiFloat4 Format for Language Model Inference

Yuanyong Luo*, Jing Huang, Yu Cheng, Ziwei Yu, Kaihua Zhang, Kehong Hong, Xinda Ma, Xin Wang, Anping Tong, Guipeng Hu, Yun Xu, Mehran Taghian, Peng Wu, Guanglin Li, Yunke Peng, Tianchi Hu, Minqi Chen, Michael Bi Mi, Hu Liu, Xiping Zhou, Junsong Wang, Qiang Lin, Heng Liao

Huawei

*Email: luoyuanyong@{hisilicon.com, yeah.net}

Abstract—This paper introduces HiFloat4 (HiF4), a block floating-point data format tailored for deep learning. Each HiF4 unit packs 64 4-bit elements with 32 bits of shared scaling metadata, averaging 4.5 bits per value. The metadata specifies a three-level scaling hierarchy, capturing inter- and intra-group dynamic range while improving the utilization of the representational space. In addition, the large 64-element group size enables matrix multiplications to be executed in a highly fixed-point manner, significantly reducing hardware area and power consumption. To evaluate the proposed format, we conducted inference experiments on several language models, including LLaMA, Qwen, Mistral, DeepSeek-V3.1 and LongCat. Results show that HiF4 achieves higher average accuracy than the state-of-the-art NVFP4 format across multiple models and diverse downstream tasks.

Index Terms—Block Floating-Point Format, Large Language Model, Deep Learning, Inference.

I. INTRODUCTION

In recent years, the rapid growth of large language models (LLMs) [1] has intensified the trade-offs among computational throughput, memory capacity, and energy efficiency [2]. These challenges have driven the community to investigate low-precision data formats as a promising solution. Several emerging 8-bit formats, including FP8 [3], HiF8 [4], [5], and MXFP8 [6], [7], have already been deployed in commercial hardware products to accelerate deep learning workloads. Yet, as model sizes and context lengths continue to expand, the exploration of low-precision formats has naturally advanced toward the 4-bit frontier. Although MXFP8, as a Block Floating-Point (BFP) format, trades off performance for training stability, BFP currently appears to be the most practical pathway for 4-bit representation. Because further reductions in bit-width can only be realized by more effectively exploiting exponent redundancy within localized data. In the following, we examine 3 influential 4-bit BFP designs outlined in Figure 1, each representing a technical advancement and introducing a new perspective.

MX4: Shared Micro-Exponents

To characterize intra-group variation, Microsoft and Meta proposed the MX4 format [8], which augments the shared 8-bit exponent [9] with 8-way 1-bit micro-exponents, forming a two-level hierarchical scaling structure. However, since MX4 uses a group size of 16, the metadata incurs a relatively high overhead of 1 bit per value. To keep the average storage below 5 bits per element, the in-group sign-magnitude format must be reduced from 4 to 3 bits, resulting in an average storage cost of 4 bits per value. This reduction ultimately causes MX4 to

deliver even lower accuracy than the vanilla 4-bit BFP format [9]. Consequently, AMD’s Versal AI Edge series adopted only the related MX6 and MX9 formats, abandoning MX4 [10]. In summary, MX4 illustrates the conceptual value of shared micro-exponents for capturing intra-group variation, yet the metadata cost — exacerbated by the small group size — prevents the format from achieving practical accuracy and efficiency.

MXFP4: Individual Micro-Exponent

OCP-MXFP4 assigns an individual 2-bit micro-exponent to each element, enabling finer intra-group variation [11]. Typically, the 4-bit in-group format is the sign-magnitude S1P2, where S denotes the sign bit, the 1 before P indicates a 1-bit integer part, and the 2 after P indicates a 2-bit fractional part (P is the binary point). This is equivalent to the common E1M2 in floating-point style, where the sign bit is usually omitted. E1M2 provides at most 3-bit significand but only a limited dynamic range of $\log_2(1.75/0.25) = 2.81$ binades. MXFP4 replaces E1M2 with E2M1, sacrificing 1 bit significand to introduce a 2-bit micro-exponent, thereby expanding the dynamic range to $\log_2(6/0.5) = 3.58$ binades. The group size is also enlarged to 32, with an average storage cost of 4.25 bits per value. MXFP4 has been adopted by several hardware vendors, including Nvidia [12], AMD [7], and Huawei [4]. However, it is now widely recognized that MXFP4 suffers from significant accuracy degradation when applied to both activations and weights [13]. As a result, it is currently employed only for weight-only quantization, as in OpenAI’s GPT-OSS [14], leaving the substantial 4-bit computing power unused. In summary, MXFP4 introduces a new trade-off between significand precision and intra-group dynamic range, but still fails to achieve the full potential of 4-bit BFP.

NVFP4: Floating-Point Scale

In addition to MXFP4, the Blackwell architecture also supports a proprietary NVFP4 format, which leverages the advantages of E2M1 over E1M2 and introduces two changes [12]. First, power-of-two scale cannot guarantee to normalize each group’s peak magnitude to the representable upper bound of E2M1, wasting intra-group dynamic range. NVFP4 replaces it with a fine-grained FP8-E4M3 floating-point scale, fully utilizing E2M1’s expressive space. Second, NVFP4 adopts the same 16-element group size as MXF4 [8], raising the average storage cost from 4.25 to 4.5 bits per value compared to MXFP4, but effectively reducing outlier-driven quantization error. Consequently, NVFP4 achieves better accuracy than MXFP4 and can be used for both weights and activations, thereby initially

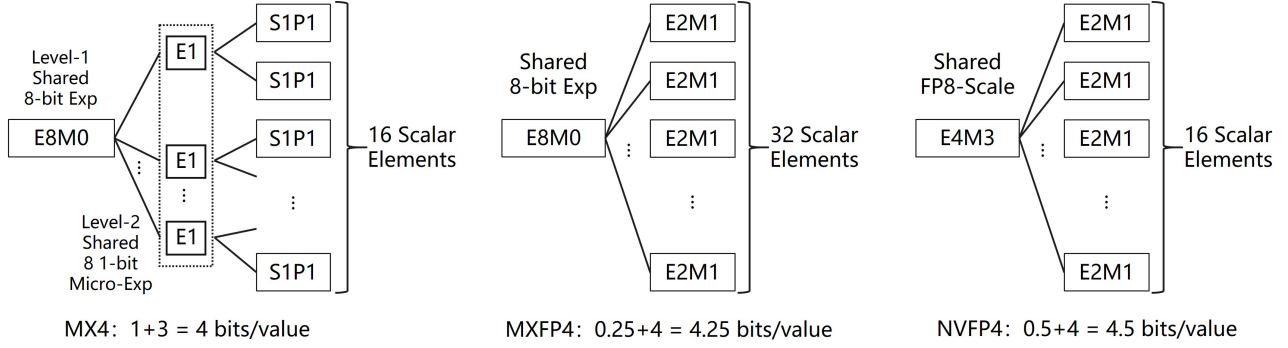


Fig. 1: The Structure of Three 4-bit Block Floating-Point Formats

unlocking practical 4-bit BFP computing power. The benefits, however, come at two heavy costs. First, the dynamic range of E4M3 is not wide enough. NVFP4 requires additional software-based per-tensor scaling (PTS) for both inference [15] and training [16], incurring performance degradation during format conversion. Second, when considering higher computing power compared to 8-bit formats, pairing a floating-point scale with a small group size leads to substantial area and power overhead in matrix-compute units. In summary, NVFP4 employs a floating-point scale to fully utilize the intra-group dynamic range, albeit with substantial hardware and software cost.

From a comprehensive standpoint, the preceding analysis underscores the inherent complexity of designing a 4-bit BFP format. MX4 and MXFP4 characterize intra-group variation using distinct micro-exponent mechanisms, while NVFP4 further emphasizes the importance of maximizing intra-group dynamic range utilization. Each approach entails trade-offs across multiple design dimensions, such as metadata overhead, group size, significand precision, and both intra- and inter-group dynamic ranges. Despite the applicability of NVFP4 to both weights and activations, its limitations in accuracy, inter-group dynamic range, and hardware efficiency remain pronounced. These shortcomings highlight the ongoing challenge of realizing practical and efficient 4-bit BFP computation.

Through multiple rounds of analysis and iteration, we identified a suitable technical entry point and proposed a new 4-bit BFP format, HiF4. Compared with the state-of-the-art, HiF4 delivers higher accuracy, broader inter-group dynamic range suitable for both inference and training, and lower hardware cost. In this paper, we describe the specification of HiF4, including the format definition and conversion. We then present comparisons of quantization error and dot-product compute flow between different 4-bit BFP formats. Finally, extensive experimental results on LLM inference are reported to demonstrate the feasibility and advantages of HiF4.

II. HiFLOAT4

This section provides a systematic description of the proposed 4-bit BFP format HiF4, and details its structural components. We then present the conversion algorithm from BF16 to HiF4, along with the suggested hardware support.

A. Format Definition

As shown in Figure 2, a basic HiF4 unit consists of 32 bits shared scaling metadata, and 64 4-bit in-group elements, resulting in an average storage of 4.5 bits per value. The following defines each component in detail.

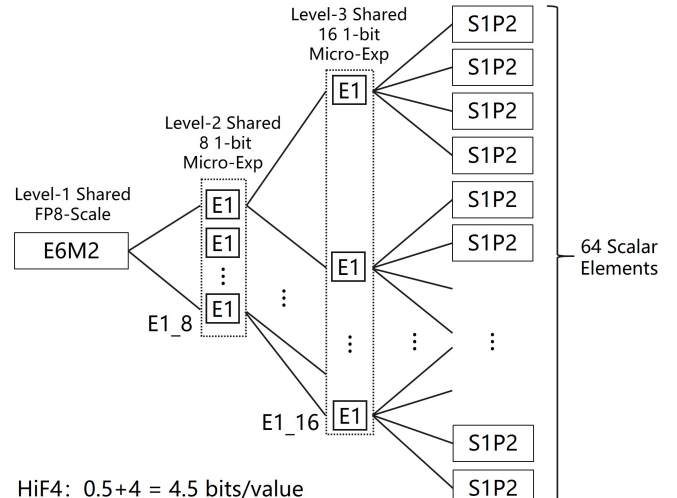


Fig. 2: The Structure of HiF4 Block Floating-Point Format

1) Scaling Metadata: The metadata defines a three-level scaling hierarchy. The first level (E6M2) is a specially designed unsigned 8-bit floating-point format. This scale provides a wide dynamic range across groups and normalizes each group's peak magnitude to the representable upper bound of the remaining hierarchical format structure, ensuring full utilization of the intra-group dynamic range. Table I summarizes the encoding details of E6M2. We assign 6 bits to the exponent field with a bias of 48, and 2 bits to the mantissa field with one hidden integer bit set to 1. E6M2 encodes NaN (Not a Number) but no other special values such as infinity or zero. Meanwhile, only normal mode is supported. Thus if we denote the unbiased exponent as E and the mantissa as M, an E6M2 number used in HiF4 should be interpreted as follows:

$$X = 2^E \times 1.M \quad (1)$$

TABLE I: E6M2 and S1P2 Encoding Details

	Unsigned FP8-E6M2	Sign-Magnitude S1P2
Exponent Bias	48	N/A
Unbiased Exp	[-48, 15]	N/A
Infinity	N/A	N/A
Zero	N/A	$S0.00_2 = \pm 0.00$
NaN	111111_11_2	N/A
Max Value	$111111_10_2 = 2^{15} \times 1.50$	$S1.11_2 = \pm 1.75$
Min Value	$000000_00_2 = 2^{-48} \times 1.00$	$S0.01_2 = \pm 0.25$

The second (E1_8) and third (E1_16) levels, implemented as 8-way and 16-way 1-bit micro-exponents, expand the intra-group dynamic range by refining local exponent differences, effectively mitigating the impact of outliers and suppressing quantization error. Micro-exponent E1 directly encodes 1 and 0, representing a very fine-grained power-of-two scaling factor. In this hierarchical scaling scheme, the level-1 E6M2 factor provides a global base scale connected to all level-2 micro-exponents. Each level-2 E1 further connects to two adjacent third-level micro-exponents, while each level-3 E1 in turn connects to four contiguous 4-bit elements within its local group. All three-level scaling metadata occupies 32 bits, distributed over 64 in-group elements, leading to an extra overhead of 0.5 bits per value.

2) *Element Encoding*: HiF4 encodes the 4-bit in-group elements using the sign-magnitude S1P2 representation. In this SXPY notation, S denotes the sign bit and P indicates the binary point. The value X preceding P designates a X-bit integer part, whereas the value Y following P designates a Y-bit fractional part. The encoding details of S1P2 are summarized in Table I. Conceptually, S1P2 is equivalent to the E1M2 format in floating-point representation; however, we adopt the S1P2 notation because it is more intuitive to interpret.

3) *Represented Values*: Since we have elaborated on each component, we can now look at the HiF4 unit as a whole and compute its represented values. As depicted in Figure 2, a single group in the HiF4 format comprises four levels of data, which are related through multiplication. Let $\{S1P2\}_i$ denote the i-th in-group element value, where $i \in [1, 64]$. Let $\{E1_8\}_j$ denote the j-th micro-exp in the level-2 scaling metadata, where $j \in [1, 8]$. Similarly, let $\{E1_16\}_k$ denote the k-th micro-exp in the level-3 scaling metadata, where $k \in [1, 16]$. Finally, let $\{V_i\}_{i=1}^{64}$ represent the 64 real numbers in a HiF4 group. Based on these definitions, each value of a HiF4 unit can be expressed as follows:

- If $E6M2 = NaN$, then $V_i = NaN$ for all $i \in [1, 64]$
- Otherwise,

$$V_i = E6M2 \times 2^{\{\{E1_8\}_{\lceil i/8 \rceil} + \{E1_16\}_{\lceil i/4 \rceil}\}} \times \{S1P2\}_i \quad (2)$$

As formulated in Equation 2, the remaining blue part — beyond the global base scale E6M2 — indicates the intra-group dynamic range that a HiF4 unit can cover: the maximum positive value is $2^{(1+1)} \times 1.75 = 7$, while the minimum positive value is $2^{(0+0)} \times 0.25 = 0.25$. Thus the available intra-group dynamic range of HiF4 is $\log_2(7/0.25) = 4.81$ binades. Some

TABLE II: Typical Values and Features for HiF4 and NVFP4

	HiF4	NVFP4
Storage Overhead	4.5 bits/value	4.5 bits/value
Group Size	64	16
Special Values	NaN and ± 0	NaN and ± 0
4-bit Element	S1P2 (E1M2)	E2M1
Significand Precision	3 bits	2 bits
Global Base Scale	E6M2	E4M3
Max Positive Value	$2^{18} \times 1.3125$	$2^{11} \times 1.3125$
Min Positive Value	2^{-50}	2^{-10}
Global Dynamic Range	[-50, 18]: 69 binades	[-10, 11]: 22 binades
Local Dynamic Range	4.81 binades	3.58 binades

typical values and features of HiF4 and the state-of-the-art NVFP4 [16] are outlined in Table II.

B. Format Conversion

Algorithm 1 illustrates the computational flow for converting a vector of 64 BF16 data into a HiF4 unit. The similar conversion procedure applies to other high-precision formats, such as FP32 and FP16.

Algorithm 1 Conversion from BF16 to HiF4

Require: A 64-length BF16 Vector: $V64$

Ensure: A HiF4 Unit: E6M2, E1_8, E1_16, S1P2_64

```

1: for  $i = 1$  to  $16$  do
2:   16 Local Peak Magnitudes:
    $V16[i] = \max(|V64[4 \times i - 3 : 4 \times i]|)$ 
3: end for
4: for  $i = 1$  to  $8$  do
5:   8 Local Peak Magnitudes:
    $V8[i] = \max(V16[2 \times i - 1 : 2 \times i])$ 
6: end for
7: Global Peak Magnitude:  $Vmax = \max(V8)$ 
8: High-Precision Scale Factor:
    $SF_{BF16} = Vmax \times (1/7)_{BF16}$ 
9: Level-1 Scale Factor:
    $E6M2 = BF16\_to\_E6M2(SF_{BF16})$ 
10: Reciprocal of E6M2:
    $E6M2\_REC = E6M2\_REC\_to\_BF16(E6M2)$ 
11: Level-2 Scale Factors:
    $E1_8 = (V8 \times E6M2\_REC \geq 4) ? 1 : 0$ 
12: for  $i = 1$  to  $16$  do
13:   Level-3 Scale Factors:  $E1_16[i] =$ 
    $(V16[i] \times E6M2\_REC \times 2^{-E1_8[\lceil i/2 \rceil]} \geq 2) ? 1 : 0$ 
14: end for
15: for  $i = 1$  to  $64$  do
16:   High-Precision Elements:  $V64\_scaled[i] =$ 
    $V64[i] \times E6M2\_REC \times 2^{-E1_8[\lceil i/8 \rceil]} \times 2^{-E1_16[\lceil i/4 \rceil]}$ 
17: end for
18: In-Group S1P2 Elements:
    $S1P2\_64 = BF16\_to\_S1P2(V64\_scaled)$ 

```

The format conversion algorithm is decomposed into three sequential stages.

Stage 1 (lines 1-7) performs a three-level tree reduction on the 64 BF16 inputs.

- In the first level, adjacent groups of 4 elements are compared in parallel, yielding 16 local maximum absolute values.
- The second level pairwise-reduces 16 maxima into 8 values.
- The final level obtains the global maximum absolute value across the 8 results.

Stage 2 (lines 8-14) derives the three-level hierarchical scaling metadata.

- Lines 8-9 compute the level-1 scale factor, in which 7 is the maximum absolute value that the intra-group structure can represent, and division by a constant is replaced by multiplication with its reciprocal to avoid performance degradation. Then a dedicated BF16 to E6M2 instruction is required to quantize the scale into E6M2 format.
- Lines 10-11 generate 8 level-2 micro-exponents, in which a bespoke reciprocal instruction that operates directly on E6M2 and returns BF16 eliminates explicit division. Then 8 parallel multiply-compare operations produce the E1_8.
- Lines 12-14 evaluate 16 level-3 micro-exponents. Observe that 2^{-E1} collapses to either 0.5 or 1. Therefore, special bypass mode of multiply instruction can be realized to compute the $BF16 \times 2^{-E1}$ value.

Stage 3 (lines 15-18) calculates the 64 in-group elements.

- Line 16 applies the three-level HiF4 scaling factors to the original 64 BF16 inputs.
- Line 18 quantizes the scaled results into S1P2 format. If the results after rounding exceed the representable range of S1P2, it should be clamped to the nearest representable bound, preserving the sign.

All rounding operations in BF16 to HiF4 conversion should use round-half-to-even or round-half-away-from-zero. Moreover, since E6M2 has no subnormal numbers, the proposed E6M2_REC_to_BF16 conversion instruction can be efficiently implemented using only a 4-entry lookup table indexed by the input 2-bit mantissa and simple exponent subtractions, to derive the output mantissa and exponent respectively. Meanwhile, some fused instructions such as multiply-compare and multiply-convert, can further accelerate the HiF4 conversion process.

III. QUANTIZATION ERROR AND DOT PRODUCT

This section first characterizes the quantization errors of different 4-bit BFP formats, then analyzes the complexity of dot product computation for HiF4 and NVFP4.

A. Quantization Error Evaluation

We generated 18 high-precision Gaussian-distributed random matrices of size 1024×1024 , each with zero mean and standard deviation $\sigma = 0.01 \times 2^x$, where $x \in [0, 17]$. Every matrix was converted to three 4-bit BFP formats. HiF4 followed Algorithm 1. MXFP4 adopted the method described in [13]. NVFP4 employed E4M3 scaling to normalize the peak magnitude of each group to 6, the representable upper bound of E2M1. Since only NVFP4 lacks sufficient dynamic range and requires additional software-based PTS, two versions were prepared for fair comparison: a direct cast and a pipeline that first scales each tensor's peak magnitude to 2688 and then quantizes to

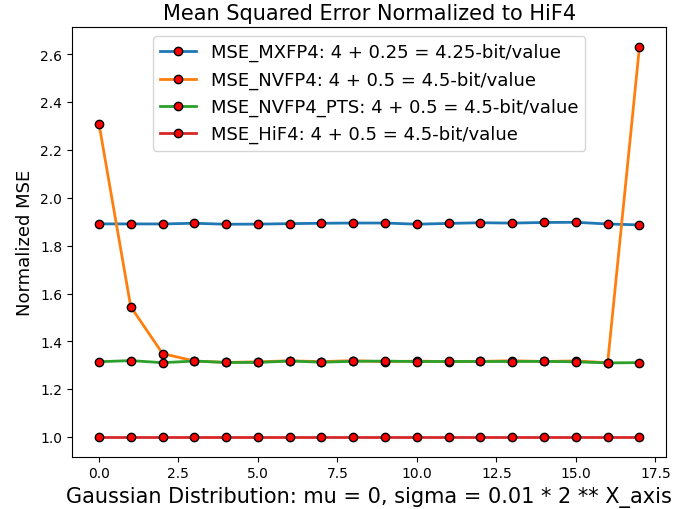


Fig. 3: Quantization Error Comparison of 4-bit BFP Formats

NVFP4 [15]. We computed the mean squared error (MSE) relative to the original high-precision matrix for each format and normalized the results with respect to HiF4.

Figure 3 depicts the quantization error of HiF4, MXFP4, and NVFP4. When data values approach the numeric bounds of NVFP4, overflow and underflow cause the quantization error to increase significantly. Applying PTS before format conversion can eliminate this precision loss. In contrast, HiF4 and MXFP4 do not require PTS, thus incurring no additional quantization overhead. Excluding NVFP4's fluctuation, the MSE ratio across the three 4-bit BFP formats remains stable:

$$\text{HiF4} : \text{NVFP4} : \text{MXFP4} = 1 : 1.32 : 1.89$$

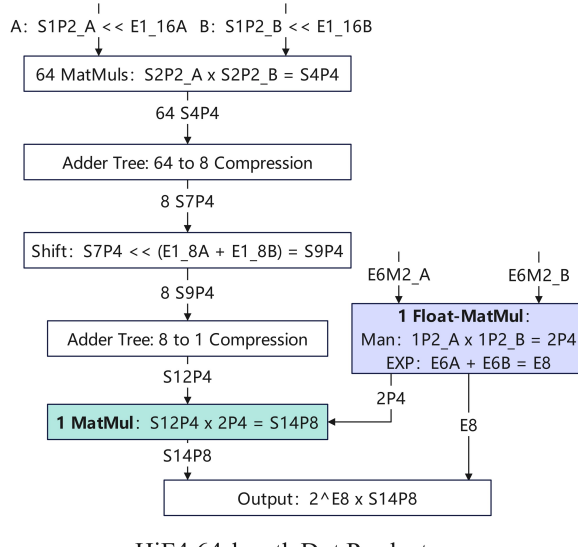
Note that although the Gaussian distribution matches the centralized nature of the data in neural networks, the quantization error may vary in practical scenarios. The experimental results serve as a quantitative reference for analyzing the accuracy of different 4-bit BFP formats.

B. Dot Product Evaluation

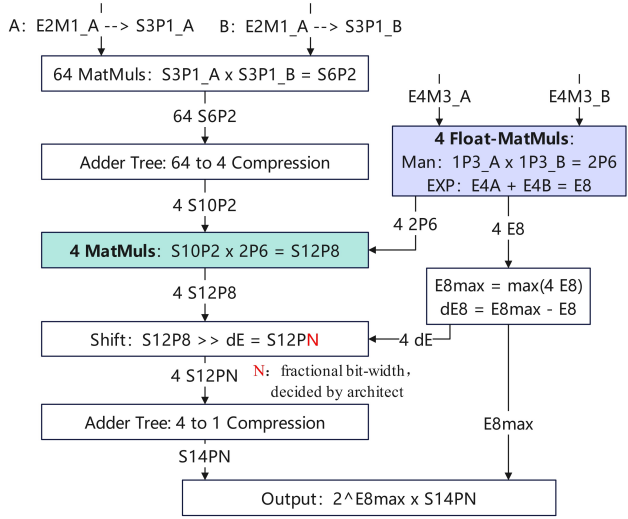
Let $A: \{E6M2^{(A)}, E1_8^{(A)}, E1_{16}^{(A)}, S1P2_{64}^{(A)}\}$ and $B: \{E6M2^{(B)}, E1_8^{(B)}, E1_{16}^{(B)}, S1P2_{64}^{(B)}\}$ denote the two HiF4 units. The dot product of A and B should be computed as follows:

$$\begin{aligned} \text{Dot}(A, B) = & E6M2^{(A)} \times E6M2^{(B)} \times \\ & \sum_{i=1}^8 2^{(E1_8^{(A)}[i] + E1_8^{(B)}[i])} \times \\ & \sum_{j=2i-1}^{2i} 2^{(E1_{16}^{(A)}[j] + E1_{16}^{(B)}[j])} \times \\ & \sum_{k=4j-3}^{4j} (S1P2_{64}^{(A)}[k] \times S1P2_{64}^{(B)}[k]) \quad (3) \end{aligned}$$

In hardware, a processing element (PE) that performs a K-length dot product and accumulation in parallel is a fundamental



HiF4 64-length Dot Product



NVFP4 64-length Dot Product

Fig. 4: Compute Flow of 64-length Dot Product for HiF4 and NVFP4

building block of matrix-compute units, such as Nvidia GPU’s Tensor Cores [17] and Ascend NPU’s Cube Cores [18]. To double the computing power of 4-bit BFP formats relative to 8-bit floating-point formats, both Tensor Cores and Cube Cores now require PEs to support 64-length dot products [4], [6]. Under these conditions, a single pair of HiF4 units suffices to match the PE input width, since their group size is exactly 64. In contrast, four pairs of NVFP4 units are required to support a 64-length dot product in a PE, because their group size is only 16. Next, we briefly analyze the compute flow of HiF4 and NVFP4 in a 64-length dot product to reveal their differences in power and area consumption.

For the HiF4 dot product, level-2 and level-3 micro-exponents can be implemented as simple left-shift operations in hardware. There are many opportunities to absorb the micro-exponents into the computations related to the S1P2 elements, depending on the implementation strategy. In our example compute flow, we directly absorb the level-3 micro-exponents into the S1P2 elements prior to multiplications. In this way, multiplier inputs become 5-bit integers, which can be denoted as S2P2 (for simplicity, we continue using the SXPY notation). Similarly, E2M1 elements in NVFP4 are converted into 5-bit integers (S3P1) before multiplications. Figure 4 illustrates the compute flow of 64-length dot product for both formats. During the compression from 64 products to a single S12P4 output, HiF4 employs pure integer arithmetic, requiring only one small floating-point multiplier and one large integer multiplier at the final stage of the accumulation tree. In contrast, NVFP4 retains integer operations only during the reduction from 64 products to four S10P2 outputs, after which four small floating-point multipliers and four large integer multipliers are required. The final accumulation from four partial results to the output is then performed entirely in floating-point. Consequently, HiF4 eliminates six multipliers and simplifies the accumulation

process compared with NVFP4.

In practice, 4-bit BFP formats are integrated into existing dot-product units originally optimized for 16-bit (FP16 and BF16) and 8-bit (INT8 and Float8) formats. Although resource sharing is feasible across different precision modes, high-precision formats do not require intermediate and final multipliers within the accumulation tree. Thus, the additional multipliers introduced by floating-point metadata E6M2 and E4M3 incur extra hardware overhead. As a result, for 64-length dot product, HiF4 occupies only approximately one-third the incremental area of NVFP4 and reduces the power consumption by about 10%. In summary, HiF4 enables a more area- and power-efficient implementation for matrix multiplication.

IV. LANGUAGE MODEL INFERENCE WITH HiFLOAT4

This section conducts a comprehensive inference evaluation of Post-Training Quantization (PTQ) across diverse tasks and LLM architectures on HiF4 and NVFP4 formats.

A. Post-Training Quantization for LLMs

To demonstrate the inherent precision of the 4-bit formats, we prioritize using HiF4 direct-cast, NVFP4 direct-cast, and the NVFP4 + PTS approach for LLM inference, as described in Section III. Meanwhile, to show that many existing PTQ methods can be adapted to enhance HiF4 accuracy with minor changes, we developed a tailored PTQ method based on the vanilla GPTQ [19], termed HiGPTQ, to exploit the fine-grained structure of the HiF4 BFP format.

B. Experiments on Small LLMs

We begin by evaluating our method on relatively smaller LLMs with the parameter size ranging from 7B to 14B. Detailed results and the corresponding inference accuracy degradation, denoted as Acc Drop, across eight benchmarks are presented in Table III. To provide an overall view of quantization errors,

TABLE III: Experimental Results of 4 Small LLMs Evaluated across 8 Benchmarks

Model	A-W Quant Type	ARC-C	ARC-E	BoolQ	HellaS	LamOp	Piqa	WinoG	MMLU	Mean
Llama2-7B	BF16	45.65	74.41	77.74	75.99	73.67	79.11	69.06	46.52	67.77
	NVFP4	44.54	73.32	76.02	75.02	73.69	77.37	70.48	41.51	66.49
	— Acc Drop	-1.11	-1.09	-1.72	-0.97	+0.02	-1.74	+1.42	-5.01	-1.28
	NVFP4+PTS	44.62	72.01	76.67	74.92	73.16	77.91	66.69	43.43	66.18
	— Acc Drop	-1.03	-2.40	-1.07	-1.07	-0.51	-1.20	-2.37	-3.09	-1.59
	HiF4	44.63	74.08	76.73	75.00	72.65	78.40	68.39	44.54	66.80
	— Acc Drop	-1.02	-0.33	-1.01	-0.99	-1.02	-0.71	-0.67	-1.98	-0.97
LLama3-8B	HiF4+HiGPTQ	45.31	73.61	76.58	74.91	73.66	77.86	68.99	43.89	66.85
	— Acc Drop	-0.34	-0.80	-1.16	-1.08	-0.01	-1.25	-0.07	-2.63	-0.92
	BF16	53.41	77.78	81.16	79.15	75.65	80.85	72.93	66.55	73.44
	NVFP4	48.04	73.74	78.35	76.56	74.21	78.56	71.43	61.64	70.32
	— Acc Drop	-5.37	-4.04	-2.81	-2.59	-1.44	-2.29	-1.50	-4.91	-3.12
	NVFP4+PTS	49.74	74.54	77.46	77.60	74.85	79.76	70.80	62.81	70.95
	— Acc Drop	-3.67	-3.24	-3.70	-1.55	-0.80	-1.09	-2.13	-3.74	-2.49
Qwen2.5-14B	HiF4	51.15	76.73	79.85	77.84	73.76	79.09	71.79	63.37	71.70
	— Acc Drop	-2.26	-1.05	-1.31	-1.31	-1.89	-1.76	-1.14	-3.18	-1.74
	HiF4+HiGPTQ	52.18	77.46	80.40	77.47	72.85	79.60	71.87	63.55	71.92
	— Acc Drop	-1.23	-0.32	-0.76	-1.68	-2.80	-1.25	-1.06	-3.00	-1.52
	BF16	58.96	79.34	85.54	82.94	74.31	81.88	74.74	80.17	77.24
	NVFP4	58.53	80.56	83.49	81.38	72.95	81.72	74.43	76.53	76.20
	— Acc Drop	-0.43	+1.22	-2.05	-1.56	-1.36	-0.16	-0.31	-3.64	-1.04
Mistral-7B	NVFP4+PTS	56.57	80.18	85.72	81.45	72.87	81.66	73.16	78.63	76.28
	— Acc Drop	-2.39	+0.84	+0.18	-1.49	-1.44	-0.22	-1.58	-1.54	-0.96
	HiF4	58.66	81.55	85.86	81.45	72.74	81.29	73.72	78.62	76.74
	— Acc Drop	-0.30	+2.21	+0.32	-1.49	-1.57	-0.59	-1.02	-1.55	-0.50
	HiF4+HiGPTQ	60.71	83.04	86.27	81.38	73.02	81.67	75.06	78.65	77.48
	— Acc Drop	+1.75	+3.70	+0.73	-1.56	-1.29	-0.21	+0.32	-1.52	+0.24
	BF16	52.39	78.37	82.17	80.50	75.14	82.21	74.11	63.30	73.52
NVFP4	NVFP4	28.41	26.30	56.09	26.69	0.0	48.69	48.30	26.79	32.66
	— Acc Drop	-23.98	-52.07	-26.08	-53.81	-75.14	-33.52	-25.81	-36.51	-40.87
	NVFP4+PTS	50.77	77.19	80.86	79.71	73.96	80.85	72.45	61.15	72.12
	— Acc Drop	-1.62	-1.18	-1.31	-0.79	-1.18	-1.36	-1.66	-2.15	-1.41
	HiF4	51.41	76.85	81.35	79.41	74.11	81.01	72.06	61.63	72.23
	— Acc Drop	-0.98	-1.52	-0.82	-1.09	-1.03	-1.20	-2.05	-1.67	-1.29
	HiF4+HiGPTQ	51.84	77.74	82.22	79.48	73.31	81.91	73.40	61.53	72.68
— Acc Drop	-0.55	-0.63	+0.05	-1.02	-1.83	-0.30	-0.71	-1.77	-0.84	

Table IV reports the average inference accuracy across all evaluated models (w/ and w/o the crashed Mistral-7B) for NVFP4, NVFP4+PTS, HiF4, and HiF4+HiGPTQ.

Models: We evaluate 4-bit quantization accuracy across a diverse collection of LLM architectures and model scales, including LLaMA2-7B [20], LLaMA3-8B [21], Qwen2.5-14B [22], and Mistral-7B [23]. These models cover a broad range of architectural designs, including Multi-Head Attention (MHA) [24] and Grouped-Query Attention (GQA) [25], as well as multiple forms of Feed-Forward Networks (FFNs) [26].

TABLE IV: Average Inference Accuracy for Small LLMs

# LLM Models	BF16	NVFP4	NVFP4+PTS	HiF4	HiF4+HiGPTQ
4 (w/ Mistral-7B)	72.99	61.42	71.38	71.87	72.23
— Acc Drop	-	Crash	-1.61	-1.12	-0.76
3(w/o Mistral-7B)	72.82	71.01	71.14	71.75	72.08
— Acc Drop	-	-1.81	-1.68	-1.07	-0.74

Datasets: We use a suite of widely adopted LLM benchmarks, including ARC-C(challenge), ARC-E(asy) [27], BoolQ [28], HellaS(wag) [29], Lam(bada)Op(enAI) [30], Piqa [31],

WinoG(rande) [32], and MMLU [33]. Together, these benchmarks span a broad spectrum of tasks, including commonsense and physical reasoning, cloze-style completion, pronoun/coreference resolution, fact verification, and multi-domain knowledge assessment.

Implementation Details: Experiments in this section are all conducted using simulated 4-bit BFP formats based on Nvidia GPU and Huawei Ascend NPU. Specifically, before matrix multiplication, all linear layer tensors (with the exception of the embedding and LLM head layers) were converted from high-precision formats only to those that could be represented in HiF4 and NVFP4 formats. All experiments reported in this sub-section were conducted in parallel on two devices. For each device, we performed three runs using different random seeds. The final results are the average inference accuracy across the three runs and both devices to ensure that random variance is minimized. For a fair comparison, we evaluate all models and quantization settings within a unified framework, in which all experiments on a given benchmark employ the same prompt template for LLM inference.

Experimental Results and Analysis: As shown in Tables III

TABLE V: Experimental Results of DeepSeek-V3.1 and LongCat Evaluated across 10 Benchmarks

Model	A-W Quant Type	ARC-C	ARC-E	BoolQ	HellaS	Piqa	WinoG	Gsm8K	MMLU	Math500	CMMLU	Mean
DeepSeek-V3.1 671B	BF16	79.91	84.44	79.76	84.41	92.93	89.34	94.46	84.86	75.00	89.28	85.44
	NVFP4	82.83	86.85	76.91	81.18	91.29	87.92	95.00	84.31	74.00	87.76	84.81
	— Acc Drop	+2.92	+2.41	-2.85	-3.23	-1.64	-1.42	+0.54	-0.55	-1.00	-1.52	-0.63
	NVFP4+PTS	81.55	87.06	77.83	81.00	91.29	88.00	95.30	84.72	78.20	87.44	85.24
	— Acc Drop	+1.64	+2.62	-1.93	-3.41	-1.64	-1.34	+0.84	-0.14	+3.20	-1.84	-0.20
	HiF4	80.86	86.89	78.87	86.60	92.44	89.11	95.75	84.77	80.20	88.71	86.42
	— Acc Drop	+0.95	+2.45	-0.89	+2.19	-0.49	-0.23	+1.29	-0.09	+5.20	-0.57	+0.98
LongCat 560B	BF16	84.38	86.64	66.85	82.09	91.46	80.27	95.91	59.19	84.80	81.65	81.32
	NVFP4	84.72	88.50	62.78	84.42	89.39	79.24	96.29	38.81	78.60	72.12	77.49
	— Acc Drop	+0.34	+1.86	-4.07	+2.33	-2.07	-1.03	+0.38	-20.38	-6.20	-9.53	-3.84
	NVFP4+PTS	87.04	89.26	63.55	84.17	89.83	79.40	95.45	39.00	78.20	72.24	77.81
	— Acc Drop	+2.66	+2.62	-3.30	+2.08	-1.63	-0.87	-0.46	-20.19	-6.60	-9.41	-3.51
	HiF4	84.98	87.95	71.19	84.04	91.19	79.56	95.75	58.03	82.60	82.74	81.80
	— Acc Drop	+0.60	+1.31	+4.34	+1.95	-0.27	-0.71	-0.16	-1.16	-2.20	+1.09	+0.48

and IV, HiF4 (direct-cast) consistently outperforms the prior state-of-the-art NVFP4 (direct-cast) and NVFP4+PTS across all four evaluated LLM models, demonstrating that the proposed HiF4 constitutes a more accurate 4-bit BFP format. We further observe that HiF4 is substantially more robust than NVFP4 under direct conversion, attributable to its larger global and suitable local dynamic ranges. For instance, Mistral-7B exhibits a broader numerical distribution, under which direct-cast inference with NVFP4 results in model failure and accuracy degradation to near random-guess levels, *i.e.*, inference crash. In contrast, HiF4 enables stable direct-cast inference under the same conditions. In addition, HiGPTQ further improves the inference accuracy of HiF4 across all four evaluated models. Notably, for the Qwen2.5-14B model, whose numerical distributions are optimized during training, the combination of HiF4 and HiGPTQ even surpasses the BF16 baseline.

In summary, the proposed HiF4 format demonstrates higher inherent precision and stability than NVFP4. Many mature PTQ methods, such as GPTQ, can be adapted with minor modifications to further enhance the accuracy of HiF4.

C. Experiments on DeepSeek-V3.1 and LongCat

Models: We further evaluate 4-bit inference accuracy on larger LLMs, DeepSeek-V3.1 (671B) [34] and LongCat (560B) [35]. These two models further encompass Multi-Head Latent Attention (MLA) and Mixture-of-Experts (MoE) architectures, which are commonly used in latest state-of-the-art LLMs.

Datasets: In addition to the benchmarks mentioned above, our evaluation suite extends to several high-stakes domains, specifically Gsm8K [36], Math500 [37] and CMMLU [38] to ensure a holistic assessment of the model’s capabilities.

Implementation Details: We deployed the LongCat and DeepSeek-V3.1 models using the vLLM framework on clusters of 32 and 64 Ascend 910B NPUs, respectively, distributed across 4 and 8 nodes. To ensure a standardized accuracy assessment, the AISBench framework was employed for evaluation. All experiments were completed within a practical timeframe. For 4-bit evaluation, we converted the tensors in the MLA_linear, MoE_linear (excluding the gating network), and FFN_linear layers to HiF4 and NVFP4 formats.

Experimental Results and Analysis: Results in Table V demonstrate that HiF4 (direct-cast) consistently surpasses the state-of-the-art NVFP4 format in 4-bit inference accuracy, including NVFP4 (direct-cast) and NVFP4+PTS. The superiority of HiF4 stems from its novel structure design as depicted in Figure 2, and more balanced features as outlined in Table II, which provide greater robustness for deep learning. For instance, HiF4 successfully handles the relatively quantization-sensitive LLM LongCat, where NVFP4 fails and leads to accuracy crashes in some hard tasks. Furthermore, in specialized cases like the DeepSeek-V3.1 model, the inherent design of HiF4 allows it to rival the BF16 baseline, highlighting its effectiveness as a high-fidelity 4-bit BFP format.

V. CONCLUSION

In this paper, we proposed a novel 4-bit BFP format, HiF4, for deep learning. Behind the design of HiF4, we first argue that E1M2 (S1P2) with 3-bit significand offers higher precision ceiling than E2M1 with 2-bit significand in the 4-bit BFP format design. Then, we successfully identified that increasing group size to 64 and employing two-level shared micro-exponents with a metadata overhead of 0.5-bit per value offers a new trade-off among overall accuracy, quantization complexity, and hardware efficiency. Additionally, we meticulously designed a dedicated global base scale that delivers sufficient inter-group dynamic range capable of directly supporting both training and inference scenarios, while enhancing the utilization of available intra-group dynamic range.

Numerical analysis shows that, compared to the state-of-the-art NVFP4 format, HiF4 reduces the MSE quantization error by 24% on Gaussian-distributed data. When 64-length dot product is integrated into existing hardware dot-product units originally optimized for 16-bit (FP16/BF16) and 8-bit (INT8/Float8) precision, HiF4 occupies only approximately one-third of the incremental area of NVFP4 and reduces power consumption by about 10%. Finally, we conducted extensive LLM inference experiments, demonstrating that HiF4 consistently achieves higher accuracy than NVFP4 across various LLM architectures and diverse tasks. Future work will present the training potential of the proposed HiF4 format.

REFERENCES

[1] H. Naveed, A. U. Khan, S. Qiu, M. Saqib, S. Anwar, M. Usman, N. Akhtar, N. Barnes, and A. Mian, “A comprehensive overview of large language models,” *ACM Transactions on Intelligent Systems and Technology*, vol. 16, no. 5, pp. 1–72, 2025.

[2] A. Gholami, Z. Yao, S. Kim, C. Hooper, M. W. Mahoney, and K. Keutzer, “Ai and memory wall,” *IEEE Micro*, vol. 44, no. 3, pp. 33–39, 2024.

[3] Nvidia, “Nvidia h100 tensor core gpu architecture,” <https://resources.nvidia.com/en-us-hopper-architecture/nvidia-h100-tensor-c>, 2022.

[4] X. Eric, “Groundbreaking superpod interconnect: Leading a new paradigm for ai infrastructure,” *Huawei Connect* 2025, <https://www.huawei.com/en/news/2025/9/hc-xu-keynote-speech>, 2025.

[5] Y. Luo, Z. Zhang, R. Wu, H. Liu, Y. Jin, K. Zheng, M. Wang, Z. He, G. Hu, L. Chen *et al.*, “Ascend float8 format for deep learning,” *arXiv preprint arXiv:2409.16626*, 2024.

[6] Nvidia, “Nvidia blackwell architecture technical brief,” <https://resources.nvidia.com/en-us-blackwell-architecture/blackwell-architecture-technical-brief>, 2025.

[7] AMD, “Amd instinct mi350x gpu brochure,” <https://www.amd.com/content/dam/amd/en/documents/instinct-technology-docs/product-briefs/amd-instinct-mi350x-gpu-brochure.pdf>, 2025.

[8] B. Darvish Rouhani, R. Zhao, V. Elango, R. Shafipour, M. Hall, M. Mesmakhosroshahi, A. More, L. Melnick, M. Golub, G. Varatkar *et al.*, “With shared microexponents, a little shifting goes a long way,” in *Proceedings of the 50th Annual International Symposium on Computer Architecture*, 2023, pp. 1–13.

[9] B. Darvish Rouhani, D. Lo, R. Zhao, M. Liu, J. Fowers, K. Ovtcharov, A. Vinogradsky, S. Massengill, L. Yang, R. Bittner *et al.*, “Pushing the limits of narrow precision inferencing at cloud scale with microsoft floating point,” *Advances in neural information processing systems*, vol. 33, pp. 10271–10281, 2020.

[10] AMD, “Versal ai edge series gen2 product brief,” <https://www.amd.com/content/dam/amd/en/documents/products/adaptive-socs-and-fpgas/versal/versal-ai-edge-gen2-product-brief.pdf>, 2024.

[11] B. D. Rouhani, N. Garegrat, T. Savell, A. More, K.-N. Han, R. Zhao, M. Hall *et al.*, “Ocp microscaling (mx) specification,” *Open Compute Project*, 2023.

[12] P. Micikevicius, “Blackwell numerics for ai,” <https://www.nvidia.com/en-us/on-demand/session/gtc25-s72458/>, 2025.

[13] B. D. Rouhani, R. Zhao, A. More, M. Hall, A. Khodamoradi, S. Deng, D. Choudhary, M. Cornea, E. Dellinger, K. Denolf *et al.*, “Microscaling data formats for deep learning,” *arXiv preprint arXiv:2310.10537*, 2023.

[14] S. Agarwal, L. Ahmad, J. Ai, S. Altman, A. Applebaum, E. Arbus, R. K. Arora, Y. Bai, B. Baker, H. Bao *et al.*, “gpt-oss-120b & gpt-oss-20b model card,” *arXiv preprint arXiv:2508.10925*, 2025.

[15] E. Alvarez, O. Almog, E. Chung, S. Layton, D. Stosic, R. Krashinsky, and K. Aubrey, “Introducing nvfp4 for efficient and accurate low-precision inference,” <https://developer.nvidia.com/blog/introducing-nvfp4-for-efficient-and-accurate-low-precision-inference/>, 2025.

[16] F. Abecassis, A. Agrusa, D. Ahn, J. Alben, S. Alborghetti, M. Andersch, S. Arayandi, A. Bjorlin, A. Blakeman, E. Briones *et al.*, “Pretraining large language models with nvfp4,” *arXiv preprint arXiv:2509.25149*, 2025.

[17] Nvidia, “Nvidia tesla v100 gpu architecture,” <https://images.nvidia.com/content/volta-architecture/pdf/volta-architecture-whitepaper.pdf>, 2017.

[18] H. Liao, J. Tu, J. Xia, and X. Zhou, “Davinci: A scalable architecture for neural network computing,” in *2019 IEEE Hot Chips 31 Symposium (HCS)*. IEEE Computer Society, 2019, pp. 1–44.

[19] E. Frantar, S. Ashkboos, T. Hoefer, and D. Alistarh, “GPTQ: Accurate post-training compression for generative pretrained transformers,” in *Proceedings of the International Conference on Learning Representations (ICLR)*, 2023.

[20] H. Touvron, L. Martin, K. Stone, P. Albert, A. Almahairi, Y. Babaei, N. Bashlykov, S. Batra, P. Bhargava, S. Bhosale *et al.*, “Llama 2: Open foundation and fine-tuned chat models,” *arXiv preprint arXiv:2307.09288*, 2023.

[21] A. Dubey, A. Jauhri, A. Pandey, A. Kadian, A. Al-Dahle, A. Letman, A. Mathur, A. Schelten, A. Yang, A. Fan *et al.*, “The llama 3 herd of models,” *arXiv e-prints*, pp. arXiv–2407, 2024.

[22] A. Yang, B. Yang, B. Zhang, B. Hui, B. Zheng, B. Yu, C. Li, D. Liu, F. Huang *et al.*, “Qwen2.5 technical report,” 2025. [Online]. Available: <https://arxiv.org/abs/2412.15115>

[23] A. Q. Jiang, A. Sablayrolles, A. Mensch, C. Bamford *et al.*, “Mistral 7b,” 2023. [Online]. Available: <https://arxiv.org/abs/2310.06825>

[24] A. Vaswani, N. Shazeer, N. Parmar, J. Uszkoreit, L. Jones, A. N. Gomez, Ł. Kaiser, and I. Polosukhin, “Attention is all you need,” *Advances in neural information processing systems*, vol. 30, 2017.

[25] J. Ainslie, J. Lee-Thorp, M. De Jong, Y. Zemlyanskiy, F. Lebrón, and S. Sanghai, “Gqa: Training generalized multi-query transformer models from multi-head checkpoints,” *arXiv preprint arXiv:2305.13245*, 2023.

[26] N. Shazeer, “Glu variants improve transformer,” *arXiv preprint arXiv:2002.05202*, 2020.

[27] P. Clark, I. Cowhey, O. Etzioni, T. Khot, A. Sabharwal, C. Schoenick, and O. Tafjord, “Think you have solved question answering? try arc, the ai2 reasoning challenge,” *arXiv:1803.05457*, 2018.

[28] C. Clark, K. Lee, M.-W. Chang, T. Kwiatkowski, M. Collins, and K. Toutanova, “Boolq: Exploring the surprising difficulty of natural yes/no questions,” in *Proceedings of the 2019 Conference of the North American Chapter of the Association for Computational Linguistics: Human Language Technologies (NAACL-HLT ’19)*. Minneapolis, MN, USA: Association for Computational Linguistics, 2019, p. 2924–2936.

[29] R. Zellers, A. Holtzman, Y. Bisk, A. Farhadi, and Y. Choi, “Hellaswag: Can a machine really finish your sentence?” in *Proceedings of the 57th Annual Meeting of the Association for Computational Linguistics (ACL)*. Florence, Italy: Association for Computational Linguistics, 2019, pp. 4791–4800.

[30] D. Paperno, G. Kruszewski, A. Lazaridou, N. Q. Pham, R. Bernardi, S. Pezzelle, M. Baroni, G. Boleda, and R. Fernández, “The LAMBADA dataset: Word prediction requiring a broad discourse context,” in *Proceedings of the 54th Annual Meeting of the Association for Computational Linguistics (Volume 1: Long Papers)*. Berlin, Germany: Association for Computational Linguistics, 2016, pp. 1525–1534.

[31] Y. Bisk, R. Zellers, R. L. Bras, J. Gao, and Y. Choi, “Piqa: Reasoning about physical commonsense in natural language,” in *Thirty-Fourth AAAI Conference on Artificial Intelligence (AAAI ’20)*, 2020, pp. 7432–7439.

[32] K. Sakaguchi, R. L. Bras, C. Bhagavatula, and Y. Choi, “Winograd: An adversarial winograd schema challenge at scale,” *arXiv preprint arXiv:1907.10641*, 2019.

[33] D. Hendrycks, C. Burns, S. Basart, A. Zou, M. Mazeika, D. Song, and J. Steinhardt, “Measuring massive multitask language understanding,” in *Proceedings of the International Conference on Learning Representations (ICLR) 2021*, 2021.

[34] A. Liu, B. Feng, B. Xue, B. Wang, B. Wu, C. Lu, C. Zhao, C. Deng, C. Zhang, C. Ruan *et al.*, “Deepseek-v3 technical report,” *arXiv preprint arXiv:2412.19437*, 2024.

[35] M. L. Team, B. Li, B. Lei, B. Wang, B. Rong, C. Wang, C. Zhang, C. Gao, C. Zhang, C. Sun *et al.*, “Longcat-flash technical report,” *arXiv preprint arXiv:2509.01322*, 2025.

[36] K. Cobbe, V. Kosaraju, M. Bavarian, M. Chen, H. Jun, L. Kaiser, M. Plappert, J. Tworek, J. Hilton, R. Nakano, C. Hesse, and J. Schulman, “Training verifiers to solve math word problems,” *arXiv preprint arXiv:2110.14168*, 2021.

[37] D. Hendrycks, C. Burns, S. Kadavath, A. Arora, S. Basart, E. Tang, D. Song, and J. Steinhardt, “Measuring mathematical problem solving with the math dataset,” in *NeurIPS*, 2021.

[38] H. Li, Y. Zhang, F. Koto, Y. Yang, H. Zhao, Y. Gong, N. Duan, and T. Baldwin, “Cmmlu: Measuring massive multitask language understanding in chinese,” 2024. [Online]. Available: <https://arxiv.org/abs/2306.09212>